

Burr, Lomax, Pareto, and Logistic Distributions from Ultrasound Speckle

Kevin J. Parker,^{1*} Sedigheh S. Poul²

¹Department of Electrical and Computer Engineering, University of Rochester

²Department of Mechanical Engineering, University of Rochester

***Corresponding Author:**

Kevin J. Parker, Department of Electrical and Computer Engineering, 724 Computer Studies Building, Box 270231, Rochester, NY, 14727-0231, USA. E-mail: kevin.parker@rochester.edu

Keywords: ultrasound, speckle, pulse-echo, fractal, vasculature

Acknowledgments and funding: This work was supported by National Institutes of Health grant R21EB025290. The authors thank Terri Swanson and Theresa Tuthill of Pfizer Inc. for providing the RF data from their liver studies. Thanks are also due to Professor Nicholas George for his profound insights on and contributions to speckle theory. The authors are grateful to Dr. R. James White and Gary Ge for the 3D vasculature data set and its rendering.

Abstract

After 100 years of theoretical treatment of speckle patterns from coherent illumination, there remain some open questions about the nature of ultrasound speckle from soft vascularized tissues. A recent hypothesis is that the fractal branching vasculature is responsible for the dominant echo pattern from organs such as the liver. In that case an analysis of cylindrical scattering structures arranged across a power law distribution of sizes is warranted. Using a simple model of echo strength and basic transformation rules from probability, we derive the first order statistics of speckle considering the amplitude, the intensity, and the natural log of amplitude. The results are given by long tailed distributions that have been studied in the statistics literature for other fields. Examples are given from simulations and animal studies, and the theoretical fit to these preliminary data support the overall framework as a plausible model for characterizing ultrasound speckle statistics.

Introduction

The study of speckle as a random interference phenomenon from coherent illumination is over 100 years old. The early work in light (predating the laser) utilized prisms to select a narrow band and study scattering¹, but even at that time the author said, “The theme of our investigation is an old one.” With the advent of radar and laser sources, the research on the mathematical properties of optical speckle were accelerated.²⁻⁸ In medical ultrasound, the mathematical treatment of speckle patterns is over 40 years in extent⁹ and has developed into a rich set of models for the statistics of backscattered echoes from tissues¹⁰.

For much of medical ultrasound, important goals include the differentiation of normal vs. pathological tissues, the detection of lesions, and the post-processing of B-scans for improved

rendering of images including computer assisted diagnosis by algorithms. All of these tasks are strengthened by a careful analysis of speckle or texture from scatterers within normal soft tissues, and then any changes associated with pathological conditions. Accordingly, over time a number of models of ultrasound speckle have been postulated, and many of these models have been adapted from earlier work from optics and electromagnetics. These models include the classical Rayleigh distribution^{9,11-13}, the K-distribution¹⁴⁻¹⁶, a Rician distribution^{6,17,18}, the Nakagami distribution¹⁹⁻²¹, a “marked model” distribution^{22,23}, and other advanced models^{24,25} with continuing applications to a variety of clinical targets²⁶⁻²⁹.

Recently, we have proposed an alternative approach to the first and second order statistics of speckle from soft vascularized tissues³⁰⁻³². Essentially, this model postulates that the fractal branching vasculature and fluid channels have an acoustic impedance mismatch of approximately 3% with respect to the surrounding tissue parenchyma. This mismatch forms the dominant set of inhomogeneities in normal soft vascularized tissues such as the prostate, thyroid, liver, and brain, and therefore the canonical scattering element is a cylinder, not a point or a sphere. Given the multi-scale, fractal structure of the vasculature, an ensemble average over all sizes from large to small leads to power law functions which propagate through different transfer functions and probability density functions (PDFs). This paper examines the first order statistics of speckle from tissue under the assumptions inherent in the framework where weak (Born approximation) scattering originates from a fractal branching set of cylindrical vessels within a reference medium and interrogated by a bandpass ultrasound pulse. It is shown that the echo amplitude, intensity, and log amplitude histograms can be modeled by conventional PDFs that are known in the statistics literature, and therefore have well described properties. These all contain a power law parameter that originates from the tissue structure itself. Preliminary examples from a 3D wave simulation

of scattering and an animal imaging study of the liver are given to demonstrate the relevance of these functions.

Theory

Spatial Convolutions and Transforms

The key assumptions and formulas used in deriving the first order statistics of speckle from a fractal branching vasculature are summarized below. First, we assume that a bandpass pressure pulse P propagating in the x direction with velocity c can be approximated by separable functions³³:

$$P\left(y, z, t - \frac{x}{c}\right) = G_y(y, \sigma_y) G_z(z, \sigma_z) P_x\left(t - \frac{x}{c}\right), \quad (1)$$

where $G_y(y, \sigma_y)$ is a Gaussian-shaped transverse beampattern in the y -direction with σ_y representing the width parameter, similar for $G_z(y, \sigma_z)$, and P_x is the propagating bandpass pulse shape in the x -direction.

Next, applying a 3D convolution model³³⁻³⁵, we assess the *dominant* echoes from the pulse interacting with each generation of elements in a branching, fractal, self-similar set of vessels shown in **Fig. 1**, and whose number density as a function of radius a follows a power law behavior³⁶ $N(a) = N_0/a^b$, where b is a real number greater than 1 defining the branching behavior of the fractal vascular tree and N_0 is a constant determining the overall number density.

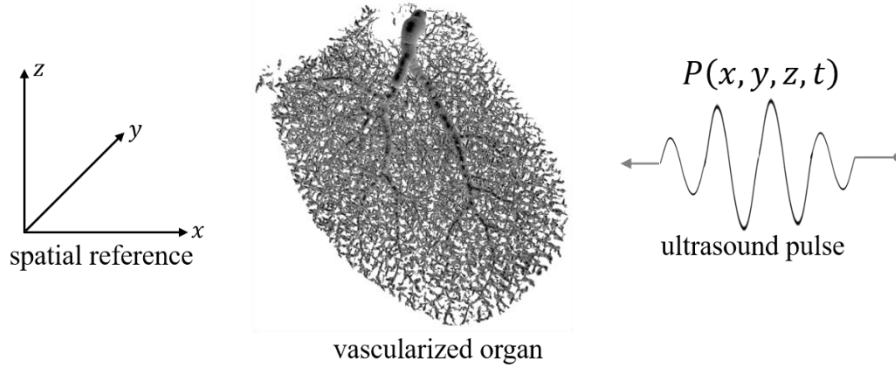


Fig. 1 Model of 3D convolution of a pulse with the fractal branching cylindrical fluid-filled channels in a soft tissue.

The canonical scatter shape for any branch is a long fluid-filled cylinder of radius a with long axis aligned along the z - direction:

$$f(r) = \begin{cases} \kappa_0 & r \leq a \\ 0 & r > a \end{cases} \quad (2)$$

$$F(\rho) = \frac{\kappa_0 \cdot a \cdot J_1[2\pi a \cdot \rho]}{\rho},$$

where κ_0 is the fractional variation in compressibility, assumed to be $\ll 1$ consistent with the Born formulation, $F(\rho)$ represents the Hankel transform using Bracewell's convention³⁷, which is the 2D Fourier transform of the radially symmetric function $f(r)$, $J_1[\cdot]$ is a Bessel function of the first kind of order 1, and ρ is the spatial frequency equal to $\sqrt{k_x^2 + k_y^2}$. The fractional variation in compressibility, κ_0 , between blood vessels and liver parenchyma has been estimated to be approximately 0.03, or a 3% difference based on published data³¹.

In addition, we also consider a “soft-walled” cylindrical vessel representing a less sharp transition in acoustic impedance between the fluid interior and the outer “solid” tissue:

$$f(r) = \frac{\kappa_0 \mathbf{e}^{-2\pi\sqrt{\left(\frac{r}{a}\right)^2+1}}}{\sqrt{\left(\frac{r}{a}\right)^2+1}} \text{ for } r > 0 \text{ and } a > 0. \quad (3)$$

Its Hankel transform is given by theorem 8.2.24 of Erdélyi and Bateman³⁸:

$$F(\rho) = \frac{\kappa_0 a^2 \mathbf{e}^{-2\pi\sqrt{(a\rho)^2+1}}}{2\pi\sqrt{(a\rho)^2+1}} \text{ for } \rho > 0 \text{ and } a > 0. \quad (4)$$

The convolution of the pulse with a cylinder of radius a is dominated by the case where the cylinder is perpendicular to the direction of the forward propagating pulse, the x - axis in our case. Thus, assuming an optimal alignment, the 3D convolution result is given by the product of the transforms:

$${}^{3D}\mathfrak{T}\{\text{echo}(x, y, z)\} = \mathfrak{T}^{3D}\{p(x, y, z)\} \cdot (k_x)^2 \mathfrak{T}^{3D}\{\text{cylinder}(x, y, z)\}, \quad (5)$$

where the $(k_x)^2$ term pre-multiplying the cylinder transform stems from the Laplacian spatial derivative in the Born scattering formulation^{39,40} and in the 3D convolution model^{35,41}.

By Parseval's theorem, the integral of the square of the transform equals the integral of the square of the echo, and provides a measure of the energy within the echo:

$$\iiint \{\text{echo}(x, y, z)\}^2 dx dy dz = \kappa_0^2 \int_{k_x=-\infty}^{\infty} \int_{k_y=-\infty}^{\infty} \int_{k_z=-\infty}^{\infty} \left(\mathfrak{T}^{3D}\{p(x, y, z)\} \right)^2 \cdot (k_x^2)^2 \cdot \left(\mathfrak{T}^{3D}\{\text{cylinder}(x, y, z)\} \right)^2 dk_x dk_y dk_z. \quad (6)$$

We assume the left side of eqn (6) is also proportional to the average intensity I of the echo as a function of the deterministic parameters on the right side, and the square root of this is proportional to the amplitude of the echo. From numerical evaluations of eqn (6) using either of two cylinders (eqn (2) or (3)) and either of two bandpass pulses (Gaussian Hermite or hyperbolic secant) we found³² an approximation which will be useful for deriving a closed form solution of

the echo amplitude A , $A[a] = A_0 \sqrt{a - a_{\min}}$ for $a > a_{\min}$, and 0 otherwise. This approximate relationship is justified by the nearly linear increase in the energy term above some minimum threshold, and the asymptotic modulus of $J_1(ak)$ which is proportional⁴² to $\sqrt{2/(\pi ak)}$ as ak becomes large. The exact shape is dependent on the particular pulse shape's spectrum and the beam pattern.

So as a working approximation, we apply the relation $A[a] = A_0 \sqrt{a - a_{\min}}$ (or for intensity I , $I[a] = I_0(a - a_{\min})$) for $a > a_{\min}$. The parameter a_{\min} depends on a number of factors, including the dynamic range selected (for example, 45 dB) and the Rayleigh scattering (long wavelength, small a) behavior of the cylinder interacting with the particular pulse transmit signal, along with the noise floor and quantization floor of the receiver.

Probability of Amplitudes

Consistent with fractal models^{36,43}, we assume that along the line of propagation of the incident pulse in Figure 1, and within the interrogated ensemble, the probability density of encountering vessels at different radii given by a power law:

$$p(a) = ((b-1)/a_{\min}) (a/a_{\min})^{-b} \quad (7)$$

for $a > a_{\min}$ and $b > 1$, and this will be transformed⁴⁴ into the probability distribution of amplitudes,

$p(A)$. The general transformation rule is:

$$p[A] = \frac{1}{dA/da} p[a]. \quad (8)$$

In our case, the derivative $dA/da = [(1/2)A_0]/\sqrt{a-a_{\min}}$, and the inverse function is $a[A] = (A/A_0)^2 + a_{\min}$. Thus, substituting these into eqn (8) the PDF $p[A]$ is:

$$p[A] = \frac{2A(a_{\min})^{b-1}(b-1)}{A_0^2 \left[\left(\frac{A}{A_0} \right)^2 + a_{\min} \right]^b}. \quad (9)$$

Furthermore, by substituting $\lambda = A_0\sqrt{a_{\min}}$, we find this reduces to a two-parameter distribution:

$$p[A] = \frac{2A(b-1)}{\lambda^2 \left[\left(\frac{A}{\lambda} \right)^2 + 1 \right]^b}, \quad (10)$$

which is a Burr Type XII distribution^{45,46} with $c = 2$. Thus, the speckle PDF is given by a two-parameter distribution with known analytic expressions for its cumulative distribution function, and moments⁴⁶. For example, the peak of the distribution occurs at $A = \lambda/\sqrt{2b-1}$ for $b > 1/2$.

Thus, the Burr distribution (10) describes the expected histogram distribution of echo amplitudes from a fractal branching set of Born cylinders. In particular, the power law parameter b is a major parameter of interest.

Probability of Intensity

For completeness, we examine the PDF of echo intensity from this model. Again, assume that the probability distribution of a fractal branching vasculature is described by a power law in radius a (a_{\min} now pertains to vessel size minimum) as given in eqn (7).

Furthermore, assume the average backscatter intensity $I(a) \cong I_0(a - a_{\min})$ for $a > a_{\min}$, zero otherwise. Then,

$$p_I(I) = \frac{p(a)}{\left(\frac{dI}{da}\right)}, \quad (11)$$

where

$$\frac{dI}{da} = I_0; \quad a = \left(\frac{I}{I_0}\right) + a_{\min}. \quad (12)$$

Thus, using the transformation rules:

$$p_I(I) = \frac{\left(\frac{b-1}{a_{\min}}\right)\left(\frac{a}{a_{\min}}\right)^{-b}}{I_0} = \frac{(b-1)}{(a_{\min})^{1-b} I_0 a^b} = \frac{(b-1)}{(a_{\min})^{1-b} I_0 \left(\frac{I}{I_0} + a_{\min}\right)^b}, \quad (13)$$

which is a Lomax distribution, also related to a Pareto type II distribution⁴⁷. This can be more compactly written as:

$$p_I(I) = \frac{(b-1)\lambda_2^{b-1}}{(I + \lambda_2)^b} \quad (14)$$

for $I > 0$ and $b > 1$, and where $\lambda_2 = I_0 \cdot a_{\min}$.

Probability of Log-Transformed Envelope

In ultrasound imaging, it is conventional to display the echo amplitudes using a log or dB scale to help with visualization of the wide dynamic range. The log transformation affects the distribution, and again using probability transformation rules⁴⁴, let $y = \ln(A)$, $dy/dA = 1/A$, and $A = e^y$. Then:

$$p_y(y) = \frac{p(A)}{dy/dA} = \frac{2(b-1)\exp[2y]}{\lambda^2 \left(\frac{\exp[2y]}{\lambda^2} + 1 \right)^b} \quad (15)$$

for $y > 0$ and $b > 1$. Note that in probability literature, this is related to the generalized logistic distribution, and for the special case where $\lambda = 1$ and $b = 2$ this becomes the sech^2 distribution⁴⁸.

Thus, each form of the received echoes from speckle {amplitude, intensity, $\ln(\text{amplitude})$ } are given by standard PDFs known in the literature {Burr type XII, Lomax, generalized logistic}. These have now been derived based on a simple transformation of probability distributions using a mapping function linking vessel radius to echo strength. However, when multiple vessels are present within the interrogating pulse, then more complex treatment is required.

Increasing Power Law b with Complex Summation

Let us assume that the interrogated sample volume in an imaging system is large enough to encompass two or several discrete cylindrical scatterers simultaneously. Because of the RF modulation of the pulse, their echo amplitudes will be complex. Because of the fractal distribution, the probability distribution of each individual reflected echo amplitude has already been given as a Burr distribution. Note that historically, the Rayleigh distribution was derived by considering a complex summation of many independent point scatterers, then by invoking the central limit theorem a Gaussian distribution is generated from the sum of many identical and independent random variables⁴⁸⁻⁵². In marked contrast in our case, we have cylindrical scatterers from a power law probability distribution over a wide range of radii, and we do not anticipate having so many vessels within a sample volume that we can invoke the central limit theorem. Furthermore, power law distributions (long tail distributions) have slow convergence to the central limit, and so it is instructive to look at the complex sum of two or few scatterers. The statistics literature has derived

the sum of random variables of these distributions but the solutions generally involve complicated generalized functions or series^{47,48,53-57}. To simplify this, we examine a complex Burr summation.

With reference to **Fig. 2**, using standard notation we can write the amplitude of the complex sum of two phasors A and B as:

$$|C| = \sqrt{(|A|\cos\theta_A + |B|\cos\theta_B)^2 + (|A|\sin\theta_A + |B|\sin\theta_B)^2}, \quad (16)$$

where $|A|$ and $|B|$ are independent Burr-distributed amplitudes (sampled from the echoes returning from the fractal branching network), and $\theta_{A,B}$ are independent and uniformly distributed over $0 \leq \theta < 2\pi$.

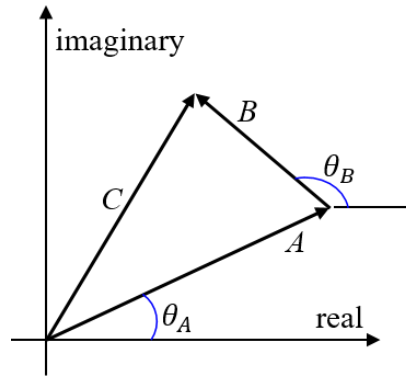


Fig. 2 The vector sum of two independent phasors, pertaining to the real and imaginary parts of a complex addition as is commonly found in models of scattering.

The new random variable $|A|\cos\theta_A$ is given by the product distribution law^{44,54} involving an integral over the PDFs for both $|A|$ and $\cos\theta_A$. By the transformation rule we can easily show that if $p(\theta) = 1/2\pi$ where $0 \leq \theta \leq 2\pi$, then $p(y = \cos\theta) = 1/(2\pi\sqrt{1-y^2})$ where $-1 < y < 1$.

Then, if $\hat{A} = |A| \cdot y$, the product distribution yields:

$$\begin{aligned}
p(\hat{A}) &= \int_{-\infty}^{\infty} p_A(A) p_y\left(\frac{z}{A}\right) \frac{1}{|A|} da \\
&= \int_{A=Z}^{\infty} \frac{4(b-1)}{2\pi(A^2+1)^b \sqrt{1-\left(\frac{z}{a}\right)^2}} dA \\
&= \frac{(b-1)\Gamma\left(b-\frac{1}{2}\right)}{\sqrt{\pi}\Gamma[b](1+\hat{A}^2)^{b-\frac{1}{2}}}
\end{aligned} \tag{17}$$

for $b > 1$ and $\lambda = 1$, where Γ is the gamma function and thus $p(\hat{A})$ is a double-sided Pearson PDF with $E[\hat{A}] = 0$.

Next we need the PDF for $|A|\cos\theta_A + |B|\cos\theta_B$. The sum of independent and identically distributed (IID) variables is given by the convolution formula⁴⁴. We found closed form solutions as ratios of polynomials for convolutions of eqn (17) only for integer orders of $b - 1/2$; it is instructive to look at one practical example. Let $Z_C = Z_A + Z_C$ with a PDF of $Z_{A,B}$ given by eqn (17), and let $b = 2.5$. Then we find:

$$p(Z_C) = \frac{4\pi(20 + Z_C^2)}{(4 + Z_C^2)^3} = 4\pi \left(\frac{20}{(4 + Z_C^2)^3} + \frac{Z_C^2}{(4 + Z_C^2)^3} \right). \tag{18}$$

The latter form emphasizes the important term with numerator 20, which dominates for $Z_C^2 < 20$ and in this example has denominator power of 3 (or more generally $b + 1/2$) Thus, the PDF of the sum of two Burr phasors' real parts is dominated by an increased power law of $b + 1/2$. In other words, the dominant power law term in the PDFs increases from 2.5 to 3. As more phasors are added, by induction this leading term increases. Specifically, a third phasor Z_C leads to another

convolution of the IID PDFs, raising the denominator power to 4 (or $b+3/2$). The final PDF of $|C|$ in eqn (16) requires further calculations and becomes complicated, however the trend towards increasing b with increasing number of cylinders is revealed by the examination of the real part of the phasor addition as given above. These PDFs are summarized in **Table 1**.

Table 1 Summary of soft tissue speckle PDFs.

Measured signal	PDF	Formula
echo amplitude A	Burr (XII)	$p(A) = \frac{2A(b-1)}{\lambda^2 \left[\left(\frac{A}{\lambda} \right)^2 + 1 \right]^b}$
echo intensity I	Lomax (Pareto II)	$p_I(I) = \frac{(b-1)\lambda_2^{b-1}}{(I+\lambda_2)^b}$
log intensity $y = \ln(A)$	Generalized logistic (II)	$p_y(y) = \frac{2(b-1)\exp[2y]}{\lambda^2 \left(\frac{\exp[2y]}{\lambda^2} + 1 \right)^b}$
phasor $\hat{A} = A \cos \theta_A$	Pearson	$p(\hat{A}) = \frac{(b-1)\Gamma\left(b - \frac{1}{2}\right)}{\sqrt{\pi}\Gamma[b](1+\hat{A}^2)^{b-\frac{1}{2}}}$
sum of independent components $Z_c = A \cos \theta_A + B \cos \theta_B$	mixed	$p(Z_c) = \frac{4\pi(20+Z_c^2)}{(4+Z_c^2)^3}$
fractal distribution of branches radius a	power law (Pareto)	$p(a) = ((b-1)/a_{\min})(a/a_{\min})^{-b}$

Methods

Simulations

In this study, to make a simple model of the liver parenchyma having vessels with fractal branching nature, a 3D block including multiscale cylindrical branches was generated to simulate the wave propagation and obtain the statistics of speckles. The block dimensions are $15 \text{ mm} \times 13 \text{ mm} \times 3 \text{ mm}$ in the axial (x), lateral (y), and transverse (z) directions, respectively, with the uniform grid element size of $69.4 \text{ } \mu\text{m}$ approximately in all directions. The distribution of the cylindrical branches as scatterers with different radii obeys the power law behavior of eqn (7) with $b = 2.5$. The cylindrical scatterers' radii ranged from 1 to 6 grid elements, and are randomly distributed in the background with no overlap among any two generated branches.

The k-Wave toolbox in MATLAB (The Mathworks, Inc., Natick, MA, USA) is employed to simulate the propagation of compressional waves in the time domain. This open-source toolbox uses the k-space pseudospectral approach to solve the acoustic wave equations.⁵⁸

Using a virtual linear array transducer defined as the source and sensor in the k-Wave toolbox, an excitation signal is applied in the form of two transient toneburst cycles with a frequency of 4 MHz. This frequency is selected to lie in the common frequency range used for adult human abdominal scanning. For the material properties assignment, the speed of sound is set to 1540 m/s and 1500 m/s for the background and scatterers, respectively, and a uniform density of 1000 kg/m^2 is assumed for the entire medium with a small absorption coefficient. Moreover, in order to avoid the reflection effect from the boundary, the 3D domain is surrounded by an absorbing boundary layer, known in the k-Wave toolbox as a perfectly matched layer, which absorbs acoustic waves at the boundaries and minimizes reflection back to the domain.

A larger study focused on the effect of the number of scatterers per unit volume from these simulations was recently completed⁵⁹ across a range of parameters including $2 < b < 3$ and further details of the simulation can be found therein.

Liver Scans

Separately, experimental results were obtained from liver experiments. Rat experiments were reviewed and approved by the Institutional Animal Care and Use Committee of Pfizer, Inc. Groton Connecticut, where the ultrasound RF data were acquired using a Vevo 2100 (VisualSonics, Toronto, CA) scanner and a 21-MHz center frequency transducer (data provided courtesy of Terry Swanson). For the purpose of examining speckle PDFs, two scans (one normal and one fibrotic) were selected for having good quality B-scan images with adequate liver ROIs. The focal depth was set to 11 mm and positioned to the lower half of the liver in the sagittal plane. In analyzing the results from simulations and liver scans, parameter estimation was performed using MATLAB nonlinear least squares minimization of error, for two-parameter fits of the Burr distribution to the data.

Results

An example from the simulation results are given in **Fig. 3**. **Fig. 3(a)** shows a 3D orientation of the transducer and random cylindrical scatterers in the domain. Only a few branches are shown here to clarify their orientation as perpendicular to the axial propagation of the interrogating pulse. **Fig. 3(b)** illustrates one realization of a random distribution of weak cylindrical scatterers of various diameters following a power law (fractal) function with $b = 2.5$ and $N_0 = 250$. **Fig. 3(c)** shows the resulting 4 MHz B-scan formed from the reflected echoes showing a characteristic speckle pattern.

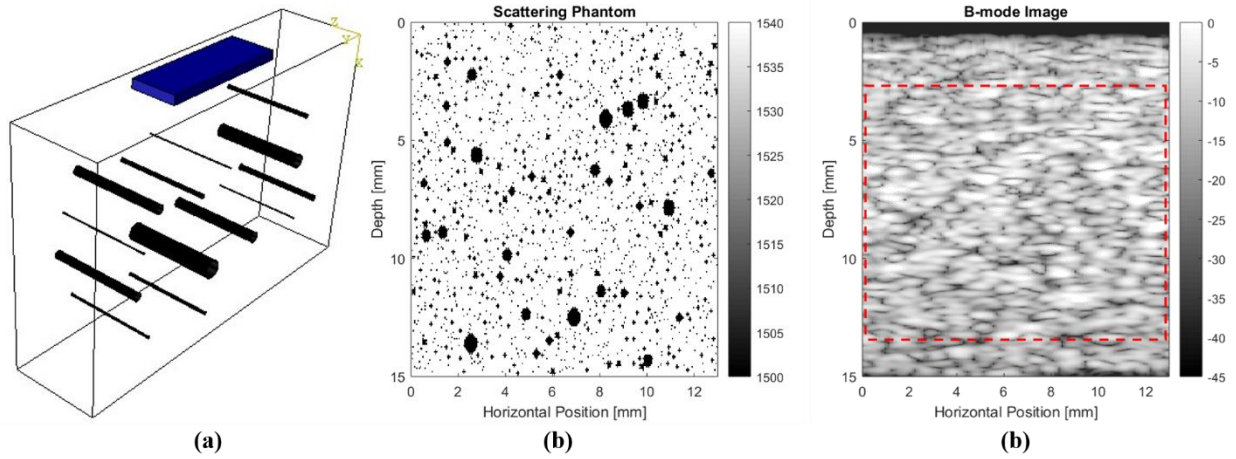


Fig. 3 (a) 3D orientation of the transducer and random cylindrical scatterers in the simulation domain. Only a few cylindrical branches are shown here to clarify their orientation as perpendicular to the axial propagation of the interrogating pulse. (b) One realization of a random distribution of weak cylindrical scatterers of various diameters following a power law (fractal) function. (c) Resulting 4 MHz B-scan demonstrating speckle pattern.

Fig. 4 contains the histograms from left to right of the amplitudes (Burr), intensity (Lomax) and log amplitude (logistic) distributions. In each case, the estimated b parameters are near 3.5, higher than the simulated $b = 2.5$. This is expected since in this simulation the estimated number of cylindrical cross sections per sample volume of the interrogating pulse is near 2.5, so the complex addition of Burr phasors acts to increase the power law above its reference value.

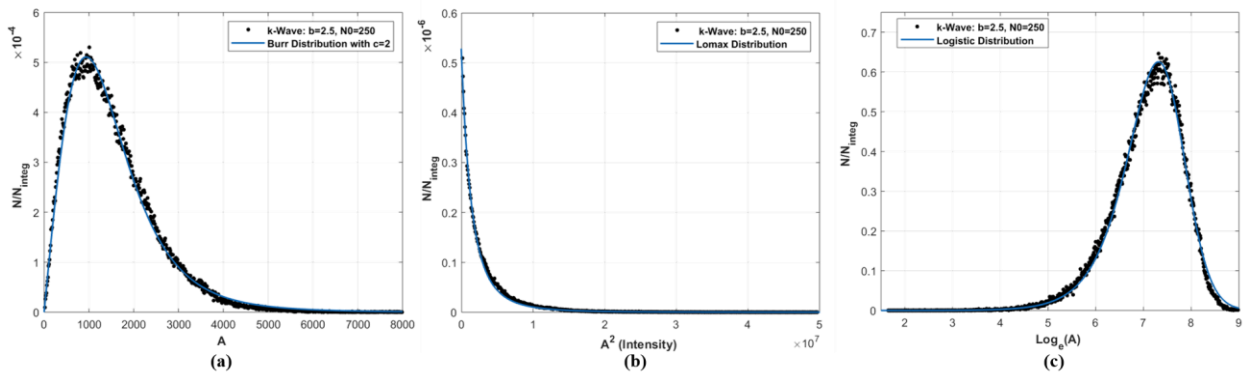


Fig. 4 Histogram curve fitting from speckle in Figure 3: (a) Burr $b = 3.357$, $\lambda = 2247$. Goodness of fit: SSE = 9.879, $R^2=0.995$. (b) Lomax $b = 3.616$, $\lambda = 5.14e+06$. Goodness of fit: SSE = 0.009627, $R^2=0.9962$. (c) Logistic $b = 3.765$, $\lambda = 2494$, Goodness of fit: SSE = 0.1784, $R^2=0.9949$.

Next, rat livers are examined and ROIs selected within the liver at a depth centered around the transmit focus at 11 mm. **Fig. 5** provides the B-scan of a normal liver, and **Fig. 6** illustrates the Burr, Lomax, and logistic fits to the associated histograms. In these cases, the power law parameters are all estimated to be around 3.8. In comparison, a rat liver from the same study but treated with CCl₄ so as to create fibrosis, is shown in **Fig. 7**. The corresponding histograms and theoretical curve fits are shown in **Fig. 8**, and in this case the estimated b parameters are not identical but range from 4.5 (Burr) to 4.9 (logistic) with the Lomax estimate intermediate at 4.7. All these b estimates are higher than those from normal livers and from the simulations, presumably due to the addition of fibrotic patches into the scattering structures of the liver.

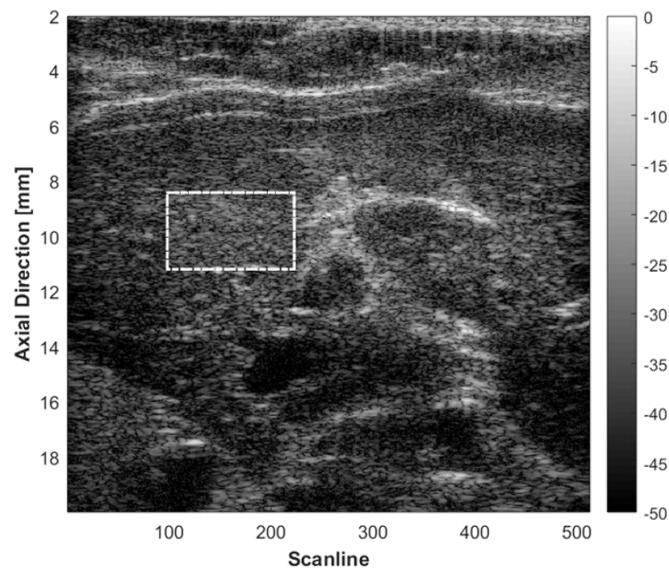


Fig. 5 Normal liver B-scan.

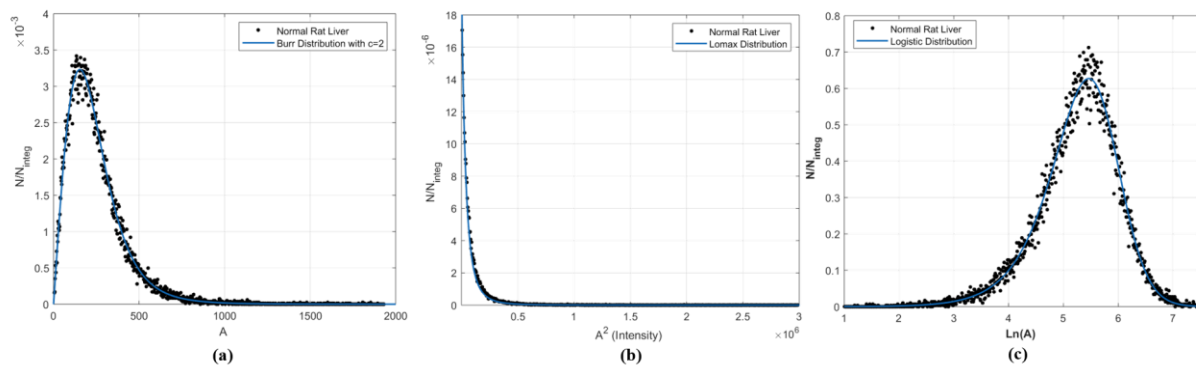


Fig. 6 Normal liver histograms from speckle in Figure 5. (a) Burr $b = 3.828$, $\lambda = 396.8$. Goodness of fit: SSE = 5.749, $R^2=0.9927$. (b) Lomax $b = 3.77$, $\lambda = 1.36e+05$. Goodness of fit: SSE = 13.22, $R^2=0.9927$. (c) Logistic $b = 3.82$, $\lambda = 395.7$, Goodness of fit: SSE = 0.4592, $R^2=0.9874$.

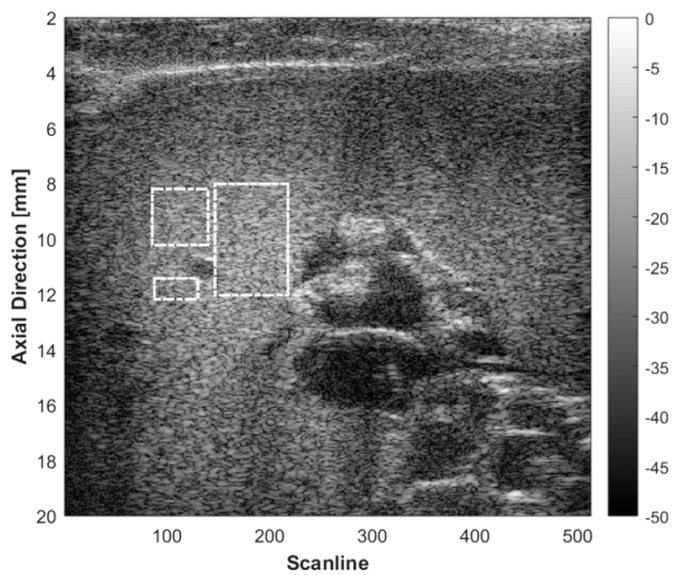


Fig. 7 Fibrotic liver B-scan.

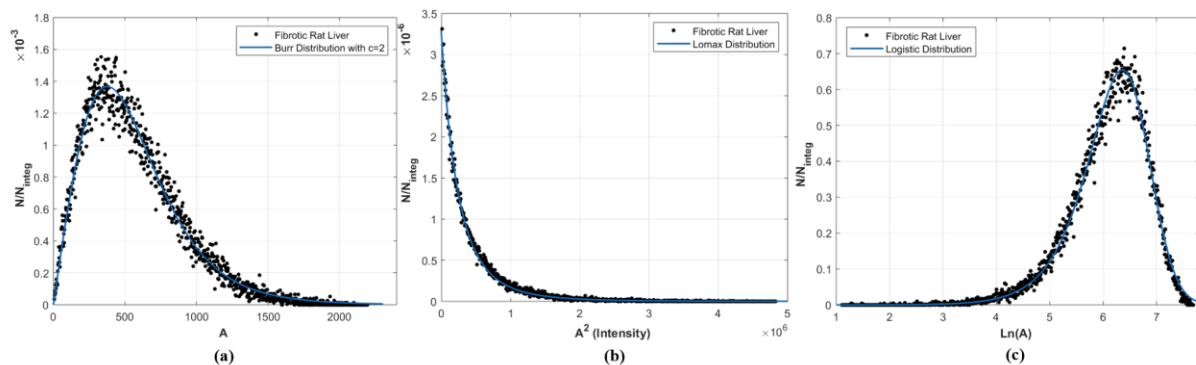


Fig. 8 Fibrotic liver histograms from speckle in Figure 7. (a) Burr $b = 4.467$, $\lambda = 1059$. Goodness of fit: SSE = 4.15, $R^2=0.9801$. (b) Lomax $b = 4.741$, $\lambda = 1.161e+06$. Goodness of fit: SSE = 1.204, $R^2=0.9946$. (c) Logistic $b = 4.955$, $\lambda = 1148$, Goodness of fit: SSE = 0.4751, $R^2=0.9881$

Discussion and Conclusion

There are several key assumptions in the derivation of the PDFs that may limit the applicability of the relationships defined in **Table 1**. First, the convolution model is only an approximation of the complicated wave propagation, but reasonably so for higher f-number focused beams³³. Furthermore, the fractal model implicitly assumes normal, soft, isotropic tissue with a simple mapping from cylinders of radius a to echo amplitude A ; the relationship is linear in intensity and single-valued over a certain range of radius compared to wavelength. This is a gross approximation, the precise details depend on the exact nature of the bandpass ultrasound pulse, but the simplified function allows straightforward transformation of probabilities. This raises the possibility that more general forms of the Burr distribution (significantly the three-parameter form of the PDF) may be useful and should be investigated further. Also, fractal models are self-similar across a wide range of scales, however any organ will have limits on the largest and smallest vessels. These limits may influence the statistics of speckle depending on the wavelength of the ultrasound pulse employed, and will require additional consideration. Another limitation is that the model implicitly assumes independent cylindrical scatterers, whereas in reality the branching vasculature is arranged in an orderly manner where each generation originates in a previous generation of vessels. The effect of this on statistics requires further analysis.

The issue of the relative merits of the three main PDFs (Burr, Lomax, and logistic) is a rich area for discussion. Since these have extensive use in the statistics literature, their behaviors are well known in terms of moments, characteristic functions, and estimators of parameters, and a lengthy catalogue of these is beyond the scope of the current discussion. However, the long tail inherent in these distributions places them all in a speckle signal-to-noise ratio of less than the Rayleigh 1.91 theoretical mean to standard deviation.⁹ In our investigations, using a minimum

mean squared error two-parameter curve fit of different data to each of these, we note that the Lomax distribution for intensity was sometimes the outlier with an elevated b estimate compared to others or compared to the baseline value used in simulations. This may be due to the pronounced concentration of the Lomax histogram near the smallest values of intensity (see **Fig. 4, 6, and 8**, middle panel), creating relative insensitivity in the curve fit to the tail of the distribution.

There is an interesting historical twist to these PDFs in that they were originally explored without any reference to ultrasound pulse echo physics. Instead, most of these are associated with economics, income distribution, and complex system lifetimes. The tie between these fields originates with the power law distribution, one of the most ubiquitous laws in natural and human phenomenon.⁶⁰ For example in the study of income distribution, a typical country would find many poor people and few rich people. In our ultrasound model, we have many small vessel branches and few large branches. Power law mathematics runs through the core formulas in both fields and then propagates through derived PDFs. Thus, we benefit from the significant work done since the 1940s in fields unrelated to ultrasound. The application of these PDFs to scans from a variety of normal and diseased tissues remains for further investigations.

References

1. M. von Laue, translated by H. K. V. Lotsch, "Sitzungsberichte der Koenig," *Pruess Akad Wiss* **47**(1144), (1914).
2. N. George, and A. Jain, "Speckle in microscopy," *Opt Commun* **6**(3), 253-257 (1972).
3. N. George, and A. Jain, "The wavelength diversity of speckle," *SPIE Developments in Laser Technology II* 161-167 (1974).

4. N. George, and A. Jain, "Space and wavelength dependence of speckle intensity," *Appl Phys* **4**(3), 201-212 (1974).
5. N. George, A. Jain, and R. D. S. Melville, "Speckle, diffusers, and depolarization," *Appl Phys* **6**(1), 65-70 (1975).
6. J. W. Goodman, "Statistical properties of laser speckle patterns," in *Laser speckle and related phenomenon* J. C. Dainty, Ed., pp. 9-75, Springer-Verlag, Heidelberg (1975).
7. J. W. Goodman, "Some fundamental properties of speckle," *J Opt Soc Am* **66**(11), 1145-1150 (1976).
8. N. George, and D. C. Sinclair, "Editor's Page: topical issue on laser speckle," *J Opt Soc Am* **66**(11), 1316-1316 (1976).
9. C. B. Burckhardt, "Speckle in ultrasound b-mode scans," *IEEE Trans Sonics Ultrason* **25**(1), 1-6 (1978).
10. J. M. Thijssen, "Ultrasonic speckle formation, analysis and processing applied to tissue characterization," *Pattern Recogn Lett* **24**(4), 659-675 (2003).
11. R. F. Wagner, S. W. Smith, J. M. Sandrik, and H. Lopez, "Statistics of speckle in ultrasound b-scans," *Ieee T Son Ultrason* **30**(3), 156-163 (1983).
12. B. J. Oosterveld, J. M. Thijssen, and W. A. Verhoef, "Texture of B-mode echograms: 3-D simulations and experiments of the effects of diffraction and scatterer density," *Ultrason Imaging* **7**(2), 142-160 (1985).
13. K. A. Wear, R. F. Wagner, D. G. Brown, and M. F. Insana, "Statistical properties of estimates of signal-to-noise ratio and number of scatterers per resolution cell," *J Acoust Soc Am* **102**(1), 635-641 (1997).

14. E. Jakeman, and R. J. A. Tough, "Generalized K distribution: a statistical model for weak scattering," *J Opt Soc Am A* **4**(9), 1764-1772 (1987).
15. G. E. Sleaf, and P. P. Lele, "Tissue characterization based on scatterer number density estimation," *IEEE Trans Ultrason Ferroelectr Freq Control* **35**(6), 749-757 (1988).
16. V. Dutt, and J. F. Greenleaf, "Speckle analysis using signal to noise ratios based on fractional order moments," *Ultrasonic Imaging* **17**(4), 251-268 (1995).
17. M. F. Insana, R. F. Wagner, B. S. Garra, D. G. Brown, and T. H. Shawker, "Analysis of ultrasound image texture via generalized Rician statistics," *Opt Eng* **25**(6), 743-748 (1986).
18. J. M. Thijssen, "Echographic image processing," in *Advances in electronics and electron physics* P. W. Hawkins, Ed., pp. 317-349, Academic Press, Boston (1992).
19. P. M. Shankar, "Ultrasonic tissue characterization using a generalized Nakagami model," *IEEE Trans Ultrason Ferroelectr Freq Control* **48**(6), 1716-1720 (2001).
20. P. M. Shankar, "A compound scattering pdf for the ultrasonic echo envelope and its relationship to K and Nakagami distributions," *IEEE Trans Ultrason Ferroelectr Freq Control* **50**(3), 339-343 (2003).
21. Z. Zhou, D. I. Tai, Y. L. Wan, J. H. Tseng, Y. R. Lin, S. Wu, K. C. Yang, Y. Y. Liao, C. K. Yeh, and P. H. Tsui, "Hepatic steatosis assessment with ultrasound small-window entropy imaging," *Ultrasound Med Biol* **44**(7), 1327-1340 (2018).
22. R. M. Cramblitt, and K. J. Parker, "Generation of non-Rayleigh speckle distributions using marked regularity models," *IEEE Trans Ultrason Ferroelectr Freq Control* **46**(4), 867-874 (1999).
23. T. A. Tuthill, R. H. Sperry, and K. J. Parker, "Deviations from Rayleigh statistics in ultrasonic speckle," *Ultrason Imaging* **10**(2), 81-89 (1988).

24. R. W. Prager, A. H. Gee, G. M. Treece, and L. H. Berman, "Analysis of speckle in ultrasound images using fractional order statistics and the homodyned k-distribution," *Ultrasonics* **40**(1-8), 133-137 (2002).
25. T. Yamaguchi, "The quantitative ultrasound diagnosis of liver fibrosis using statistical analysis of the echo envelope," in *Quantitative Ultrasound in Soft Tissues, Chapter 11* J. Mamou, and M. L. Oelze, Eds., pp. 275-288, Springer Netherlands, Dordrecht (2013).
26. F. Destrempes, and G. Cloutier, "A critical review and uniformized representation of statistical distributions modeling the ultrasound echo envelope," *Ultrasound Med Biol* **36**(7), 1037-1051 (2010).
27. Z. Klimonda, P. Karwat, H. Piotrkowska-Wróblewska, K. Dobruch-Sobczak, and J. Litniewski, "Ultrasound scattering statistics predicts the result of neoadjuvant chemotherapy of breast tumors at an early stage of treatment," *2019 IEEE International Ultrasonics Symposium (IUS)* 1512-1514 (2019).
28. A. Tang, F. Destrempes, S. Kazemirad, J. Garcia-Duitama, B. N. Nguyen, and G. Cloutier, "Quantitative ultrasound and machine learning for assessment of steatohepatitis in a rat model," *Eur Radiol* **29**(5), 2175-2184 (2019).
29. R. Hu, R. Singla, F. Deeba, and R. N. Rohling, "Acoustic shadow detection: study and statistics of B-mode and radiofrequency data," *Ultrasound Med Biol* **45**(8), 2248-2257 (2019).
30. K. J. Parker, J. J. Carroll-Nellenback, and R. W. Wood, "The 3D spatial autocorrelation of the branching fractal vasculature," *Acoustics* **1**(2), 369-381 (2019).
31. K. J. Parker, "Shapes and distributions of soft tissue scatterers," *Phys Med Biol* **64**(17), 175022 (2019).

32. K. J. Parker, "The first order statistics of backscatter from the fractal branching vasculature," *J Acoust Soc Am* **146**(5), 3318-3326 (2019).
33. A. Macovski, *Basic Ultrasonic Imaging*, Prentice-Hall, Englewood Cliffs, N.J. (1983).
34. J. L. Prince, and J. M. Links, *Medical imaging signals and systems*, 2., [updated] ed., Pearson, Boston (2015).
35. J. C. Bamber, and R. J. Dickinson, "Ultrasonic B-scanning: a computer simulation," *Phys Med Biol* **25**(3), 463-479 (1980).
36. T. Vicsek, *Fractal growth phenomena*, 2nd. ed., World Scientific, Singapore (1992).
37. R. N. Bracewell, "The Fourier transform and its applications, chapter 12," in *The Fourier transform and its applications, chapter 12*, McGraw-Hill, New York (1965).
38. A. Erdélyi, and H. Bateman, *Tables of integral transforms. vol. 2*, New York, McGraw-Hill (1954).
39. L. Rayleigh, "On the scattering of light spherical shells, and by complete spheres of periodic structure, when the refractivity is small," *Proceedings of the Royal Society of London. Series A* **94**(660), 296-300 (1918).
40. P. M. Morse, and K. U. Ingard, *Theoretical Acoustics, Chapter 8*, Princeton University Press, Princeton, NJ (1987).
41. J. C. Gore, and S. Leeman, "Ultrasonic backscattering from human tissue: a realistic model," *Phys Med Biol* **22**(2), 317-326 (1977).
42. M. Abramowitz, and I. A. Stegun, *Handbook of mathematical functions with formulas, graphs, and mathematical tables*, U.S. Govt. Print. Off., Washington, (1964).
43. J. J. Carroll-Nellenback, R. J. White, R. W. Wood, and K. J. Parker, "Liver backscatter and the hepatic vasculature's autocorrelation function," *Acoustics* **2**(1), 3-12 (2020).

44. A. Papoulis, *The Fourier integral and its applications*, McGraw-Hill, New York (1987).
45. I. W. Burr, "Cumulative frequency functions," *Ann Math Stat* **13**(2), 215-232 (1942).
46. R. N. Rodriguez, "A guide to the Burr type XII distributions," *Biometrika* **64**(1), 129-134 (1977).
47. M. H. Tahir, G. M. Cordeiro, M. Mansoor, and M. Zubair, "The Weibull-Lomax distribution: properties and applications," *Hacet J Math Stat* **44**(2), 455-474 (2015).
48. N. Balakrishnan, *Handbook of the logistic distribution*, Dekker, New York (1992).
49. D. Middleton, *An introduction to statistical communication theory*, McGraw-Hill, New York, (1960).
50. J. C. Kluyver, "A local probability problem," *Proc Royal Netherlands Academiby of Arts and Sciences (KNAW)* **8**(1), 341-350 (1905).
51. J. A. Greenwood, and D. Durand, "The distribution of length and components of the sum of n random unit vectors," *Ann Math Stat* **26**(2), 233-246 (1955).
52. M. M. Siddiqui, "Some problems connected with Rayleigh distributions," *J Res Nat Bur Stand D* **66D**(2), 167-174 (1962).
53. S. Nadarajah, "Exponentiated Pareto distributions," *Statistics* **39**(3), 255-260 (2005).
54. S. Nadarajah, and M. M. Ali, "Pareto random variables for hydrological modeling," *Water Resour Man* **22**(10), 1381-1393 (2008).
55. S. Nadarajah, "Exact distribution of the product of m gamma and n Pareto random variables," *J Comput Appl Math* **235**(15), 4496-4512 (2011).
56. Q. H. Nguyen, and C. Robert, "Series expansions for sums of independent Pareto random variables, <http://docs.isfa.fr/labo/2012.16.pdf>," Lyon (2013).

57. W. Abu-Dayyeh, A. Assrhani, and K. Ibrahim, "Estimation of the shape and scale parameters of Pareto distribution using ranked set sampling," *Stat Papers* **54**(1), 207–225 (2013).
58. B. E. Treeby, and B. T. Cox, "k-Wave: MATLAB toolbox for the simulation and reconstruction of photoacoustic wave fields," *J Biomed Opt* **15**(2), 021314 (2010).
59. K. J. Parker, and S. S. Poul, "Speckle from branching vasculature: dependence on number density," *arXiv preprint arXiv:2002.05623* (2020).
60. M. E. J. Newman, "Power laws, Pareto distributions and Zipf's law," *Contemp Phys* **46**(5), 323-351 (2005).